Three-dimensional pore structure visualization and characterization of paper using X-ray computed tomography

YVES DEFRENNE, VASILI ZHDANKIN, SAHANA RAMANNA, SHRI RAMASWAMY, AND BANDARU V. RAMARAO

ABSTRACT: Porous biomaterials such as paper and board have a complex structure that influences their mechanical, optical, and transport properties and thereby their performance during manufacturing and end uses. Reconstruction of the three-dimensional (3D) pore spaces in paper was obtained by X-ray computed tomography and used to study the structure and its impact on properties. A set of laboratory-made paper samples of varying freeness was prepared, and the 3D structures of the samples were visualized and characterized. Tomographic reconstruction images were processed using techniques such as anisotropic diffusion, minimum error thresholding, and isolated voxel removal to enhance image quality. The pore structures were analyzed to determine porosity, fiber-pore interfacial surface area, geometric tortuosity, and pore size distributions (using a sphere growing algorithm). These properties were compared with experimental data and were found to be in good agreement. The results from 3D visualization and characterization were then compared with experimental data of various samples using conventional pore structure characterization techniques, such as mercury intrusion porosimetry.

Application: Image processing techniques can help mills better understand the complex structure of porous biomaterials that influences properties and performance of manufactured products.

Porous biomaterials such as wood and paper have a complex three-dimensional (3D) structure consisting of interconnected pores and cellulose fibers. The understanding of this structure is important in determining the structural characteristics and properties of such materials. Previously, conventional characterization techniques, such as microscopy, energy dispersive X-ray spectroscopy [1,2], and mercury intrusion porosimetry (MIP) [3,4], were used. These techniques concentrate mainly on the 2D structure visualization; they are invasive and do not provide complete structural information. Mercury intrusion porosimetry is a conventional intrusive experimental technique used to characterize the porous materials. Hence, 3D characterization techniques were explored. X-ray computed tomography (XRCT) is one such technique that provides excellent visualization at micron and submicron scale [5-9]. X-ray computed tomography has been used increasingly to characterize the structure of porous materials [9-12]. Bloch et. al. have used XRCT to evaluate structural properties such as porosity, permeability, and effective thermal conductivity in paper and other porous materials [5,9,12]. Van Den Bulcke et al. and Mayo et al. used XRCT to investigate the structure of wood [7,8,13]. Antoine et al. used phase contrast X-ray tomography to obtain high quality images of paper structures [14]. Noninvasive techniques such as XRCT make it possible to visualize and characterize the structure of materials without any potential changes during the measurement. The principle of computed tomography is based on capturing a series of images of the object by rotating along a single or a dual-tilt axis. Using the tilt series, a 3D reconstruction is carried out by a back-projection technique [15].

In our previous work, low resolution XRCT images were used to visualize the 3D structure of paper and determine its pore characteristics [16-18]. The current work focuses on high resolution XRCT images of different paper samples acquired from the European Synchrotron Radiation Facility (ESRF; Grenoble, France). A series of effective image processing steps was applied to ensure maximum noise reduction while preserving the essential features of the images. Techniques such as anisotropic diffusion, minimum error thresholding, and isolated voxel removal were used to yield high quality images with clear distinction between the pore and fiber phases. A noninvasive method to determine the 3D pore size distribution and porosity, fiber-pore interfacial surface area, and geometric tortuosity is presented. The results from 3D visualization and characterization are then compared with experimental data of various samples using conventional techniques such as MIP.

MATERIALS AND METHODS

Paper samples

A large pool of samples of different varieties of paper was selected for our analysis. They included 300 g/m^2 paper handsheets made using softwood bleached kraft pulp (SWBK) fiber refined to different levels according to TAPPI T-205

"Forming handsheets for physical tests of pulp"; these were characterized by CSF levels in the range of 220–670 mL. Other samples consisted of varying types of fiber furnish with fibers obtained from different raw material sources (e.g., hardwood and softwood). Finally, commercial paper samples were subjected to calendering (mechanical densification of a dry paper sample) treatment and those that contained inorganic fillers (denoted as samples 1, 2, and 3).

X-ray computed tomography

High resolution XRCT images were obtained at ESRF using the ID 19 beamline (http://www.esrf.eu/home/UsersAndScience/find-a-beamline.html). This beamline was specifically designed for parallel beam applications by placing the very small (<100 µm) source 145 m away from the sample being scanned. Monochromaticity is ensured by a multilayer coated X-ray optical device with a narrow bandwidth. The pixel size was chosen to be 0.7 µm to provide a large enough field of view that would still retain a balance of high resolution in the scanned sample. The energy of the X-rays was 20 keV. With a resolution of 2048 x 2048 pixels, the samples to be scanned were about 1.4 mm wide and 1.4 mm tall. In about 20 min, a total of 1500 radiographs, over 180°, were taken. In the sample preparation process, a thin acrylic capillary tube was dipped into a hot adhesive and then instantly applied to the front of a cut piece of a sticky note with the same dimensions as the sample to be scanned. The sticky side was then gently pressed onto the sample. The reconstruction was done by a back projection technique [19].

Image processing

Even though the fibers are clearly identifiable (**Fig. 1**), the lack of sufficient contrast in XRCT images makes the automated recognition of each of these fibers difficult to implement. To enable the automated separation and identification of these two phases, an algorithm based on the following image processing techniques was developed and implemented in the following sequence:

1. Smooth only the regions of similar grayscale intensities.
2. Preserve edges or interfaces between different phases in the material.
3. Conduct adaptive smoothing, taking into account surrounding local image characteristics.
4. Generate a binary image.

Anisotropic diffusion

The technique of anisotropic diffusion filtering is an adaptive smoothing technique that preserves the edges or interfaces between two different phases in the material [9,20]. It is based on simulating the diffusion of a tracer inside an anisotropic medium, and the diffusivity is represented by a direction dependent tensor [20]. The rate of change of the voxel intensity, I, is given by the divergence of the local intensity gradient (Eq. 1):

$$\frac{\partial I}{\partial t} = div(c(x,y,z,t)\nabla I) = c(x,y,z,t)\Delta I + \nabla c.\nabla \mathrm{I} \quad (1)$$

where I is the voxel intensity, c represents the diffusion coefficient, t is the time during iteration, and ∇I is the grayscale gradient.

The grayscale intensities between two consecutive iterations of the filter are related by [19] (Eq. 2):

$$I(x,y,z,t+1) = I(x,y,z,t) + \frac{1}{n}\sum_i \sum_j \sum_k w(i,j,k)\, c3\big(\nabla I(i,j,k)\big)\, \nabla I(i,j,k) \quad (2)$$

where w is the weighing coefficient, if implemented; n is the number of voxels taken into account; and i, j, and k are integers in a certain interval [-d, +d] such that the length of the vector (i,j,k) is lesser than the mask radius.

The diffusion coefficient $c3$ was chosen to be directly proportional to the grayscale gradient given by the following exponential function (Eq. 3):

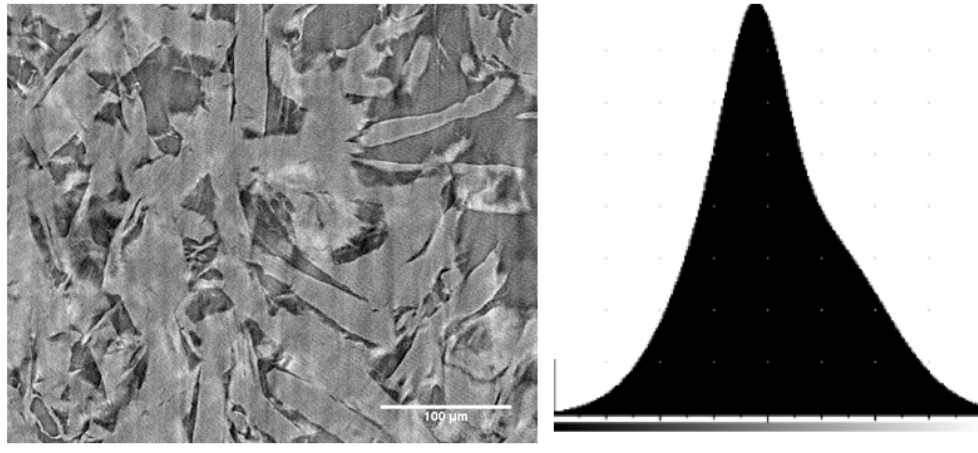

1. Zoomed-in region (left) and histogram of a slice from a high resolution raw image stack.

$$c3 = exp\left[-\left(\frac{\|\nabla I\|}{K}\right)^4\right] \quad (3)$$

K was chosen as 60 and 30 for the first and second iterations, respectively, to ensure quick denoising without affecting the edges. For the rest of the iterations, *K* was constant and chosen to be 14. The value of *K* is dependent on the image to be processed. The convergence criterion employed for ending the filtering process for classifying voxels was less than 5% between successive iterations.

The anisotropic diffusion filter resulted in a histogram with two distinct Gaussian distributions corresponding to the two phases. The surface plots also revealed noise elimination and smoothing while retaining the features of the interface.

Thresholding

Once the anisotropic diffusion resulted in a histogram where two different peaks could be identified, a minimum error thresholding method was used to classify the pore and fiber phases [21,22]. The minimum error threshold method fitted two normal distributions to the overall histogram data. The point of intersection of these two curves was chosen as the threshold, as shown in **Fig. 2**. The threshold value ensured that the sum of the misclassified voxels in either phase was minimal. The misclassified voxels are located in the area under the curve on either side of the threshold value.

Final filtering steps

Even with the anisotropic diffusion method, some voxels that have unusually large or small grayscale values as compared with their neighbors cannot be smoothed out and could end up being misclassified. Hence, an isolated voxel removal algorithm was applied to detect and label all of the disconnected or isolated groups of voxels; their volumes were compared with a predetermined threshold volume. The threshold volume (512 μm³) (8 μm x 8 μm x 8 μm) was chosen because all the fiber voxels were expected to be connected and the smallest isolated cellulose fiber particle (i.e., fines) was defined to be about 75 μm. If the isolated voxel volume was below the threshold volume (512 μm³), then it was removed.

After the isolated voxels were eliminated, a morphological operator was applied to compensate for potential surface roughness misrepresentation caused by noise. The dilation and erosion algorithms were applied [22] and combined to yield either an open or a closed filter. It was found that five consecutive dilate steps followed by five erode steps were optimal in the current work. Once these final filtering steps were completed, the images were ready to be used for the determination of structural and transport characteristics.

Determination of pore structural characteristics

Once the images were filtered and binarized, pore structural characteristics such as porosity, fiber-pore interfacial specific surface area (SSA), geometric tortuosity and 3D pore size distribution could be determined.

Porosity

Porosity was one of the simplest measurements because the images contained two separate phases that have been identified. The porosity of the sample was calculated as (Eq. 4):

$$\varepsilon = \frac{number\ of\ pore\ voxels}{total\ number\ of\ voxels} \quad (4)$$

The porosity obtained from XRCT images of paper samples was verified with the experimentally obtained porosity based on sheet thickness (caliper) and basis weight (weight per unit area) measurements and also by MIP. The basis weight measurements were obtained by taking a sample of rectangular shape, measuring its dimensions (x,y), determining thickness using a caliper (z), and weighing the sample. Basis weight was calculated as follows (Eq. 5):

$$Basis\ weight = \frac{Weight}{A_{total}} \quad g/m^2 \quad (5)$$

The apparent density was calculated as follows (Eq. 6):

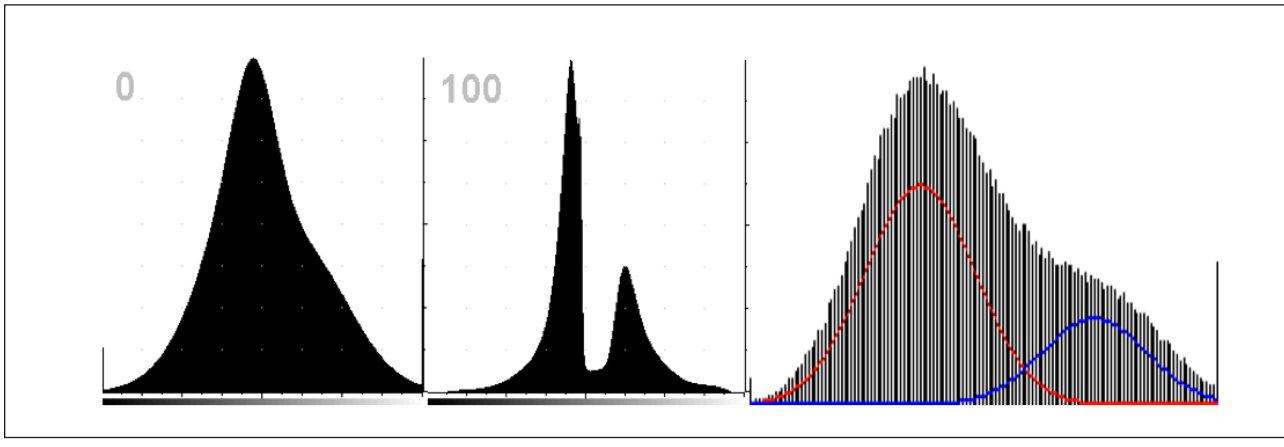

2. Histogram before (left) and after anisotropic diffusion (middle) and minimum error thresholding method (right).

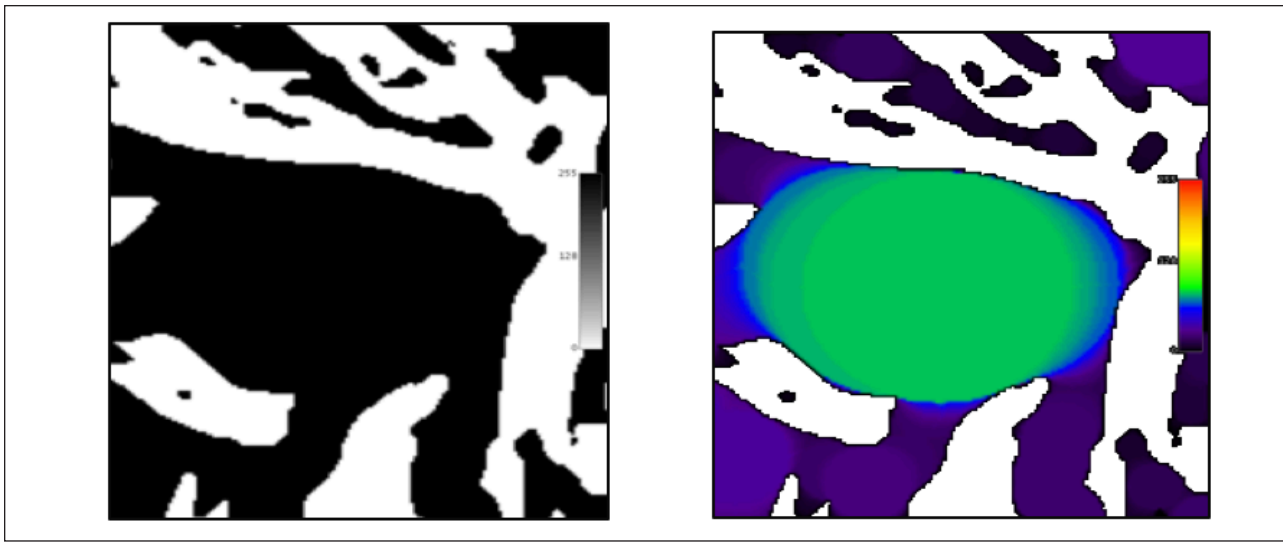

3. Cross section of the processed image before (left) and after (right) fitting spheres.

$$\rho_a = \frac{Basis\ weight}{z} \qquad g/m^3 \tag{6}$$

The cell wall density of the cellulose fiber (ρ_f) was taken to be 1.55 g/cm^3 under normal conditions [23]; hence the volume of fiber was calculated as follows (Eq. 7):

$$V_{fiber} = \frac{weight}{\rho_f} \tag{7}$$

The porosity is then calculated as follows (Eq. 8):

$$\varepsilon = \frac{V_{total} - V_{fiber}}{V_{total}} = \frac{(1/\rho_a - 1/\rho_f)}{1/\rho_a} \tag{8}$$

Specific surface area

The total interfacial area, S_t, was determined by counting the number of voxels that correspond to the pore-fiber interface and then multiplying that by the face area (square) of a cubic voxel. The SSA or the interfacial area per unit mass, S_W (m^2/g), and specific area per unit volume, S_V (m^2/m^3), can be given by (Eqs. 9 and 10):

$$S_W = \frac{S_t}{(1-\varepsilon)\rho_f} \qquad m^2/g \tag{9}$$

$$S_V = \frac{S_t}{1-\varepsilon} \qquad m^3/g \tag{10}$$

where S_t is the total interfacial area, ε is the porosity, and ρ_f is the fiber density.

3D pore size distribution

Given that fibrous, porous materials have complex 3D structures, characterizing them using 2D approximations have inherent limitations. In the 2D model, long narrow pores are approximated using equivalent circular pores and their equivalent pore dimensions are then calculated. Also, 2D methods do not take into account important structural information in the third dimension. Hence, to get a more complete and accurate characterization of the porous network, a 3D characterization of the pore size distribution is necessary. This was achieved using a sphere growing algorithm.

In the sphere growing algorithm, a diameter map was created for the porous structure. This involved fitting a sphere of maximum size at every pore voxel location. Spheres were grown inside the pore space starting with a diameter of one and incrementing the diameter until it encountered a fiber voxel. This will give the maximum sphere diameter at that location and is then repeated for the entire volume. Once the diameter map was obtained, full spheres were grown starting from the smallest diameter and ending at the largest. As larger spheres are grown, they take over any voxels they overlap from previously grown smaller spheres. Then, the volume of pore space corresponding to the maximum sphere at a given location and its distribution gives the pore size distribution for the structure. **Figure 3** shows the cross section of the processed image before and after fitting spheres.

Tortuosity

In addition to classical structural parameters such as porosity, surface area, and pore size distribution, another important structural characteristic is tortuosity. In porous materials such as paper and board, the interfiber capillaries can be highly tortuous. There are two different aspects of tortuosity: (1) geometric tortuosity, defined by geometric features, and (2) transport (i.e., diffusion) tortuosity, deduced from resistance offered to fluid flow and mass transport in porous media. In this paper, we report a method to characterize the geometric tortuosity using the actual 3D structures of porous materials. Geometric tortuosity is defined as the ratio of the actual length of the pore space (capillaries between the fibers) to the straight line (or

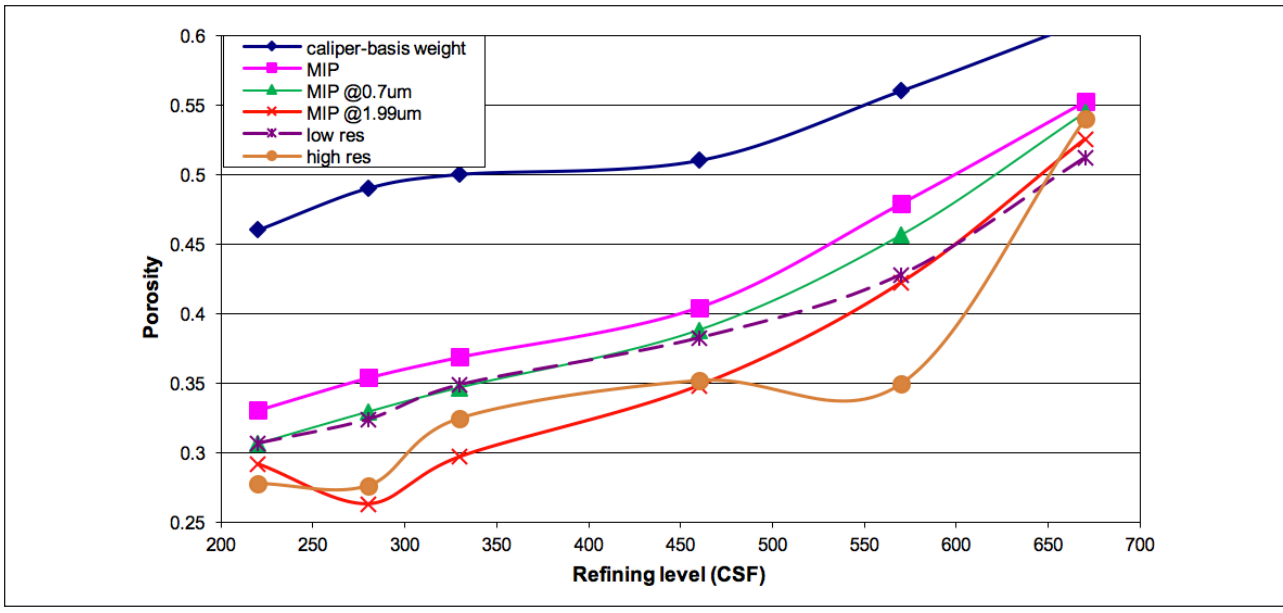

4. Effect of refining level on porosity of softwood bleached kraft (SWBK) handsheets obtained by different methods

the shortest length) of the capillary [24]. It is more meaningful to determine the overall average geometric tortuosity for an entire volume. The algorithm we developed is based on allowing walkers (particles) to pass through the pores in a 3D image of the sample. Starting off on one face of the sample image, the tracers are allowed to traverse through the structure predominantly in one direction (i.e., in-plane and transverse directions). It is thus possible to obtain independent measurements of in-plane and transverse geometric tortuosity.

Mercury intrusion porosimetry

Pore structure characterizations using XRCT and image analysis were compared with experimental data obtained with MIP. Mercury intrusion porosimetry is a common, invasive method used to evaluate structural characteristics such as pore volume and pore size distribution of porous materials [25,27]. The method is based on the principle that the pressure required to force a nonwetting liquid to fill the pores inside the material is inversely proportional to the diameter of the pores [28]. The relationship between the pore diameter and pressure was established using the Lucas Washburn equation [29]. Using the Lucas Washburn equation and the known values of surface tension and contact angle for mercury, the relationship between pore diameter (D, m) and applied pressure (P) can be given as (Eq. 11):

$$D = \frac{213}{P} \quad (11)$$

RESULTS AND DISCUSSION

For the pool of paper samples, various structural properties such as porosity, SSA, 3D pore size distribution, and tortuosity were determined with the help of XRCT images of the corresponding samples, as well as experimental methods.

Porosity and specific surface area

Porosity results obtained from image analysis of XRCT images taken at high resolution (0.7 µm), were compared with porosity measurements based on sheet thickness and basis weight as well as mercury intrusion porosimetry, for paper samples with varying mechanical treatment or refining levels as measured by freeness (CSF, mL) . The results were also compared with low resolution XRCT images (2 µm) that were used in the previous work [30]. CSF is a measurement of the extent of mechanical treatment given to cellulose fibers prior to papermaking. The level of mechanical treatment or refining the pulp has undergone influences the swelling of fibers, strength, surface area, density, and amount of open space between the fibers when formed into a sheet [31]. The CSF of a paper sample decreases with the amount of mechanical treatment. With increase in the extent of refining, fiber cell walls are separated (defibrillation), which extends the fibrils on the fiber surface. When formed into a sheet, this causes an increase in the density and hence lowers the porosity as freeness decreases. The densification of the structure as evidenced by a decrease in porosity is shown by all the methods studied (**Fig. 4**). Apparent density measured by sample basis weight and thickness is a gross measurement; as expected, this exhibited the highest value for all the samples. MIP porosity values were greater than those obtained by image analysis. This could be because of the ability of MIP to detect pores much smaller than the resolution capability of XRCT.

Given the heterogeneity of paper structures and small sample volumes used on XRCT, there is an inherent variability in the structural characteristics [32]. To obtain a reasonable average for a larger sample, it is thus necessary to evaluate a number of regions within a sample volume. Whenever possible, three repeats of the sample scans from different locations were conducted. As shown in **Fig. 5**, the average varia-

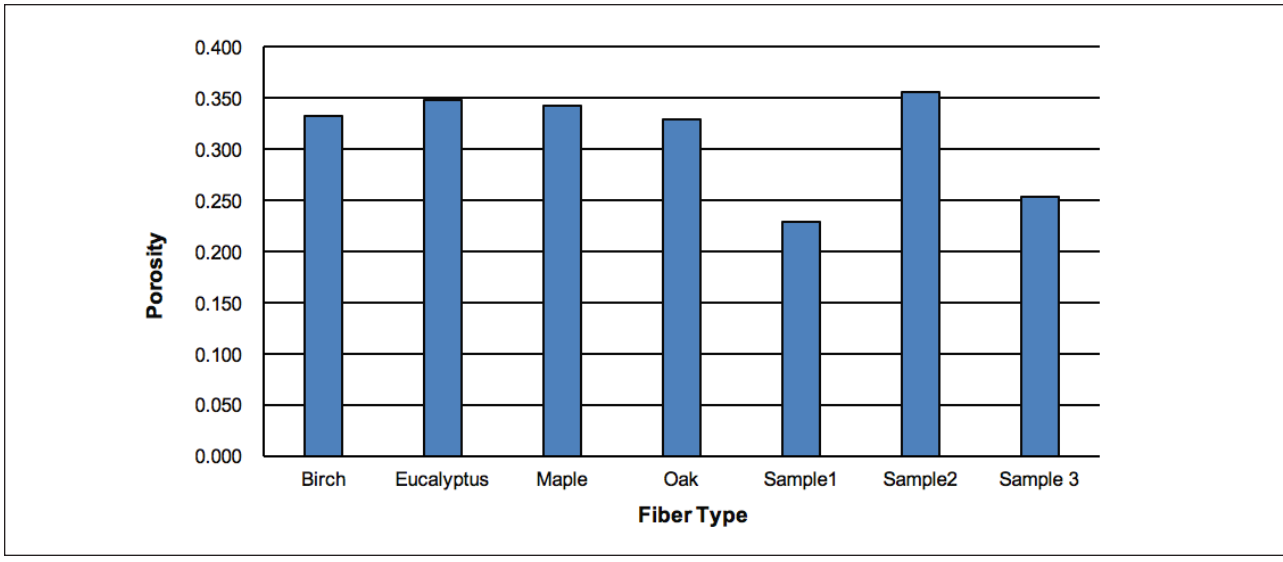

5. Porosity comparison for different fiber furnishes (laboratory handsheets) and commercial samples.

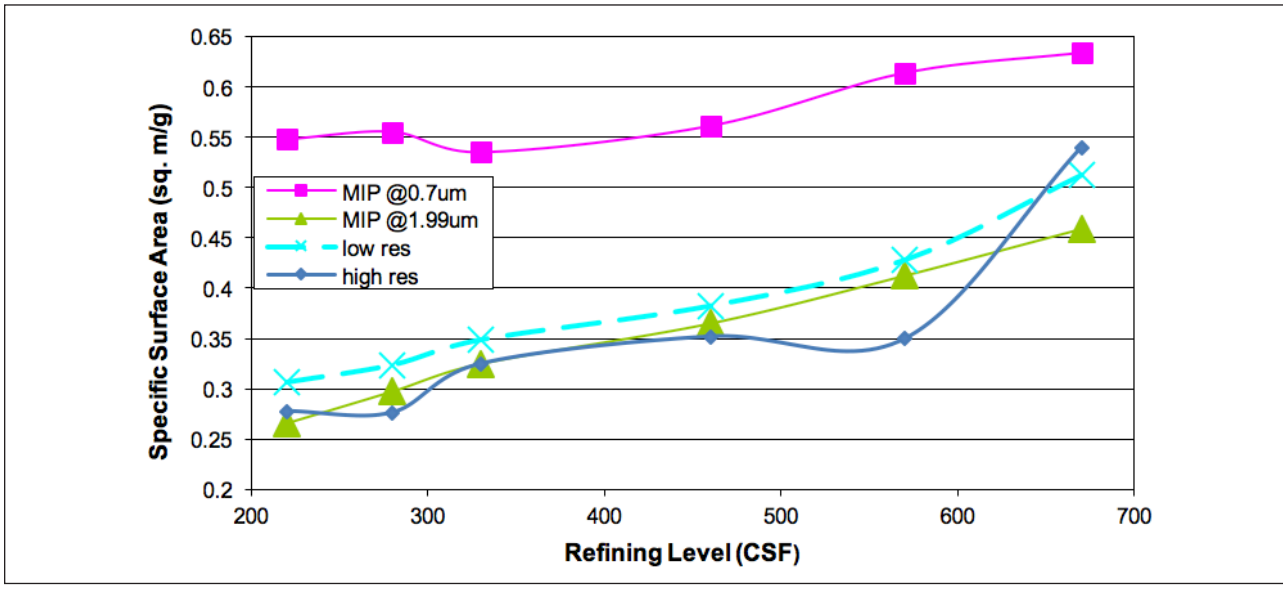

6. Effect of refining on specific surface area of SWBK handsheets obtained by different methods.

tion in structural characteristics measured using XRCT and image analysis for a given sample taken from various locations (normally three to five locations for a given sample) is about ±1%–14%. Taking this into consideration, the noninvasive XRCT technique does capture the changes in porosity as a result of mechanical treatment of fibers.

Figure 5 shows a similar comparison of paper structures made using cellulose fibers from different wood species, such as oak, birch, eucalyptus, and maple, and three commercially made fine paper samples, identified as samples 1, 2, and 3. It is again observed that the commercially made samples subjected to standard densification processes of wet pressing and calendering mostly exhibited a lower porosity than laboratory-made handsheets.

The SSA results for paper samples of different refining levels obtained by image analysis were compared with results obtained by MIP. As in the case of porosity, SSA results by MIP were much larger than those by image analysis. However, when the total MIP results were analyzed, considering only up to pore sizes of 0.7 μm and 1.99 μm, they were closer to the image analysis results. Even though the surface area of individual fibers increases with increases in the level of mechanical treatment due to defibrillation, the trend is opposite in the case of dry paper samples (**Fig. 6**). This is because the individual fibers are compacted and collapsed to form paper sheets, which increases the density and reduces the porosity as well as the exposed nonbonded interfacial area.

Similar comparisons for different fiber species and commercial samples also show a decrease in SSA with a higher degree of densification and consolidation (**Fig. 7**). The commercially made paper samples mostly show a lower surface

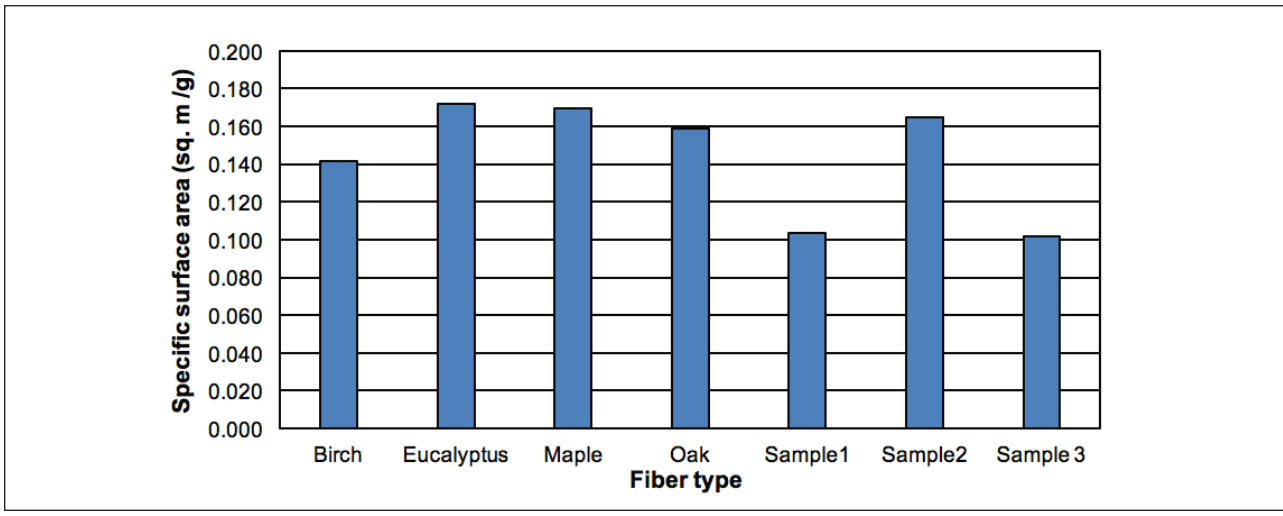

7. Specific surface area comparison for different fiber furnishes (laboratory handsheets) and commercial samples.

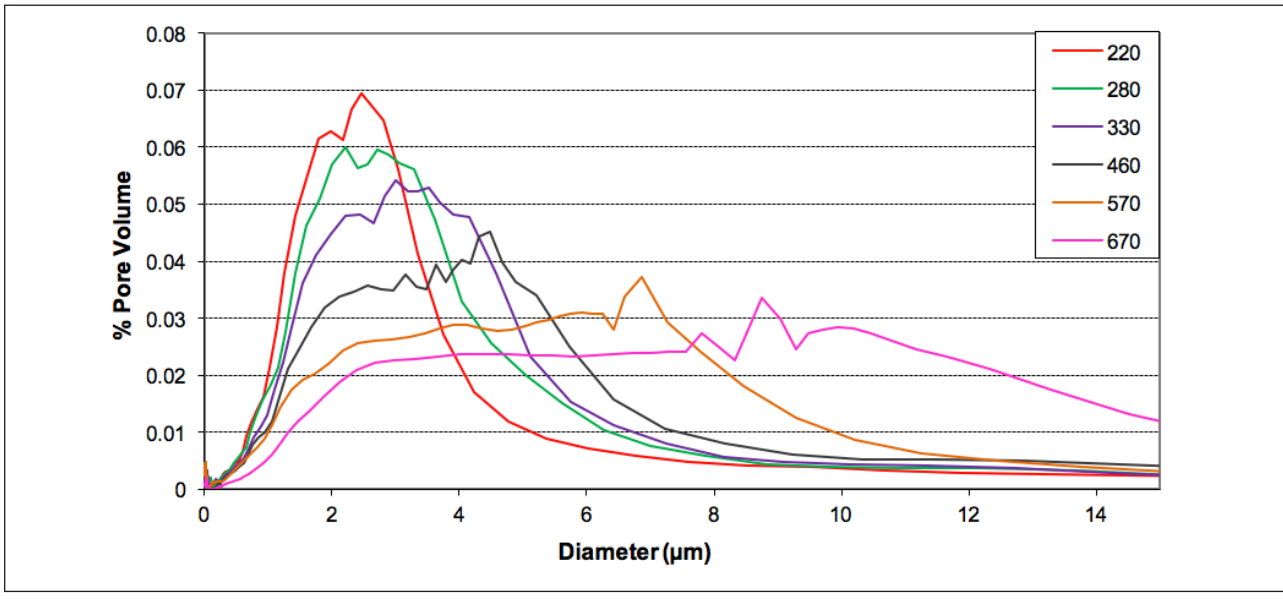

8. Three-dimensional pore size distributions of SWBK handsheets at different refining levels obtained from mercury intrusion porosimetry (MIP).

area compared with the laboratory-made handsheets, which is consistent with the porosity data.

3D pore size distribution and tortuosity

The sphere growing algorithm was used to compute the 3D pore size distributions from high and low resolution XRCT images and compare them with the results obtained from MIP. **Figure 8** shows the pore size distributions obtained from MIP for samples with different levels of refining. As shown in Fig. 8, as the degree of mechanical refining of fibers is increased, the initially larger pores with wider distribution shift toward smaller pores and narrower distribution. This is expected because of the densification and consolidation of the structure, as shown by the porosity data. Because of the nature of the MIP technique, there is also a significant contribution to the size distribution from very small pores. In addition to being able to access really small pores, part of the volume from small pores can also be attributed to potential misinterpretation because of the ink-bottle effect [27].

A similar effect of refining on the pore size distribution is also observed with results from XRCT images obtained using the high resolution and low resolution methods as shown in **Figs. 9 and 10**. In the case of XRCT images, because of the limits of resolution and pixel size, pore diameters below 0.7 µm and 4 µm cannot be detected for the high and low resolution images, respectively. Hence the high peak near smaller diameters that was observed in the case of MIP is not visible here. Similar to MIP, with increasing refining and consolidation of the structure, there is a shift toward smaller pores and narrower mean pore diameter.

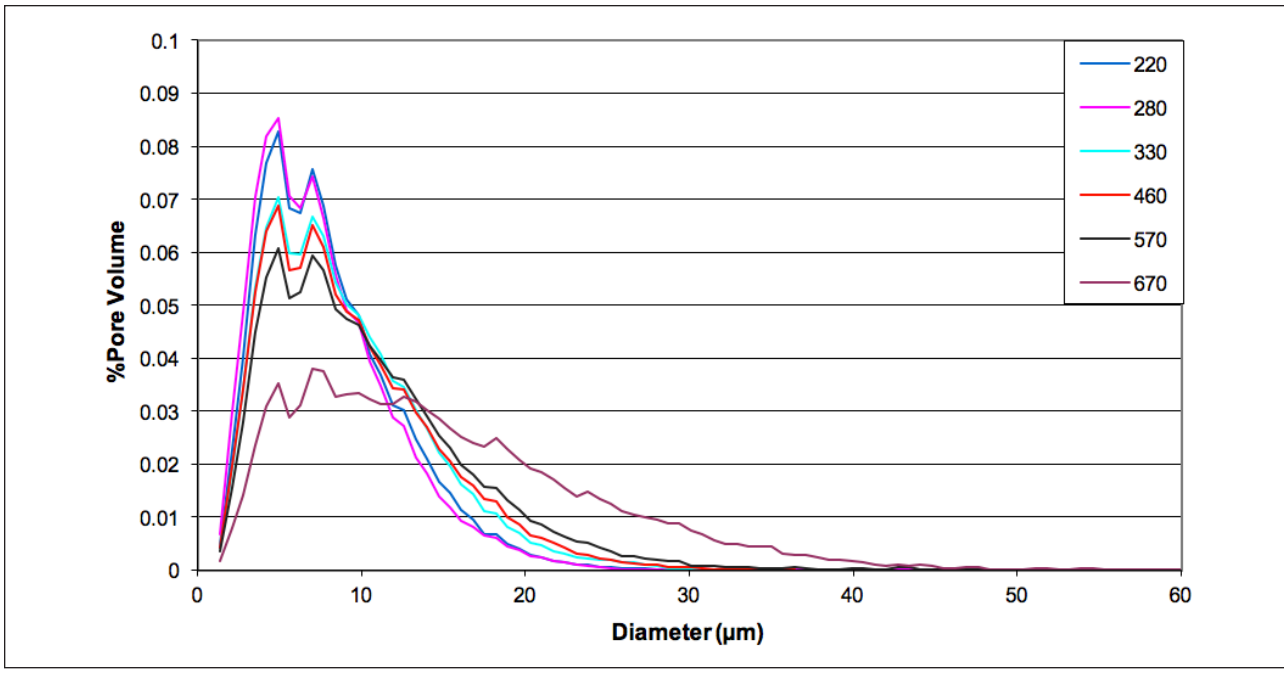

9. Three-dimensional pore size distributions of SWBK handsheets at different refining levels for high resolution X-ray computed tomography (XRCT) images computed by sphere growing method.

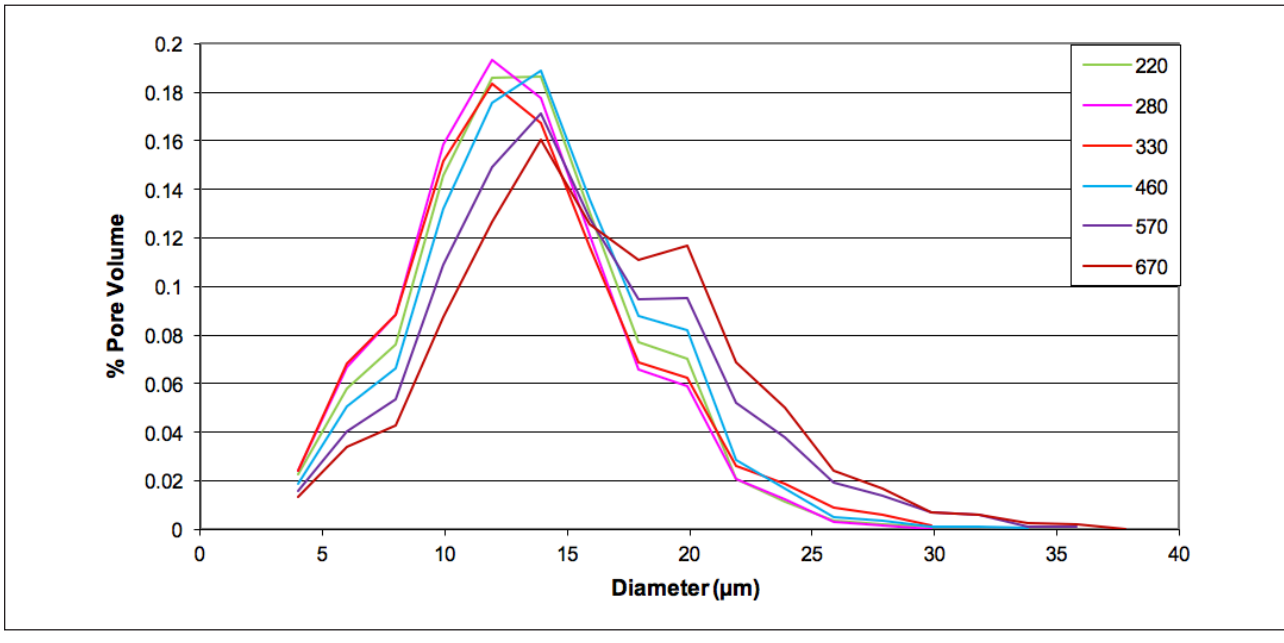

10. Three-dimensional pore size distributions of SWBK handsheets at different refining levels for low resolution XRCT images computed by sphere growing method.

The lower resolution images show a much bigger and broader pore size distribution. Even though decreasing mean pore size with increasing refining can be observed, in general the average pore size for low resolution images is about twice that of high resolution images for the same samples. The low resolution technique is quite coarse and only capable of capturing larger pores and hence might not be suitable for some of the end uses of paper. **Figures 11 and 12** show the comparison of pore size distributions obtained using different techniques (i.e., MIP and high and low resolution XRCT) for the same refining level (460 and 670 CSF, respectively). The MIP technique shows pore size distribution in the smallest pore size range followed by 3D high and low resolution XRCT images (**Fig. 13**).

Two-dimensional in-plane and transverse pore size distributions using the equivalent hydraulic diameter approach

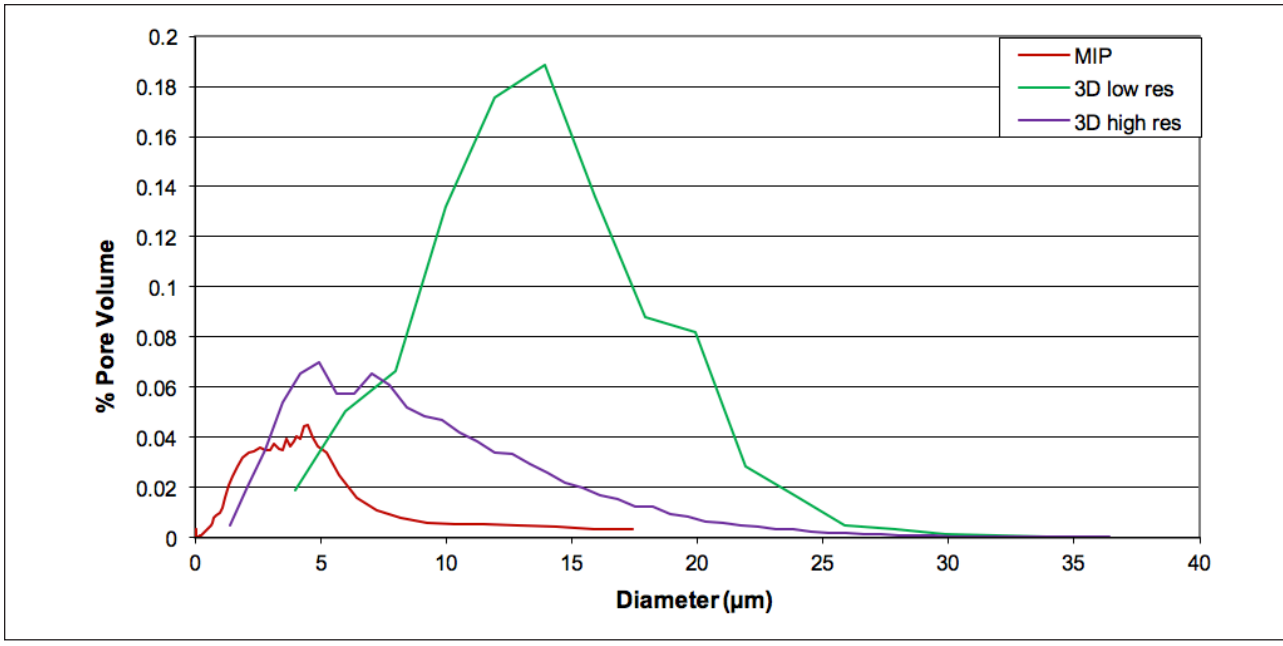

11. Comparison of 3D pore size distribution results for 460 CSF sample obtained by MIP and high resolution and low resolution XRCT images.

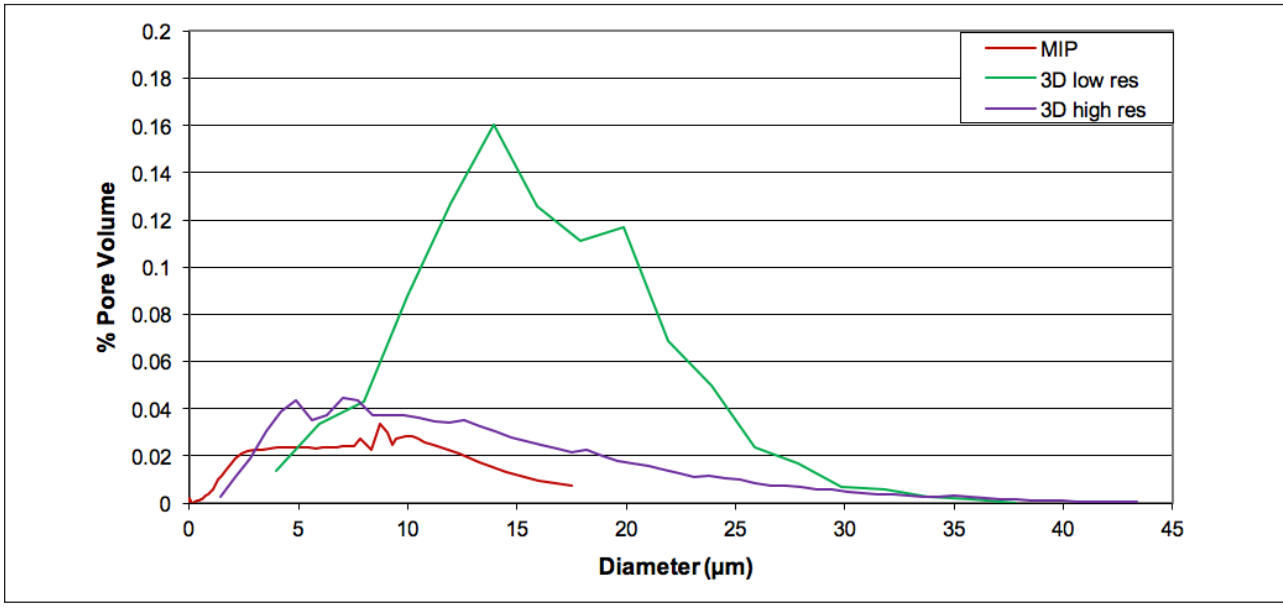

12. Comparison of 3D pore size distribution results for 670 CSF sample obtained by MIP and high and low resolution XRCT images.

were also determined for the high and low resolution XRCT images for comparison. In comparison with 3D pore size distribution results, 2D results showed bigger pore sizes. This is because the third dimension is not taken into account, which might contribute to decreasing the pore size. Moreover, the 3D pore size distributions are a combination of the in-plane and transverse pore size distributions. It was observed that the equivalent pore sizes in the plane (in-plane) direction were always lower than those in the transverse direction because the fibers are mostly aligned horizontally during papermaking and then formed layer by layer. Even though the pore sizes in the in-plane direction appear to be smaller than those in the transverse direction, it has been experimentally shown that in-plane liquid permeability in paper samples is always greater than transverse permeability [33]. This apparent anomaly can be explained further by studying the geometric tortuosity, which is also known to contribute to the overall resistance to flow. On the basis of these discussions, the 3D pore size distribution method is preferred for characterizing pore size distribution

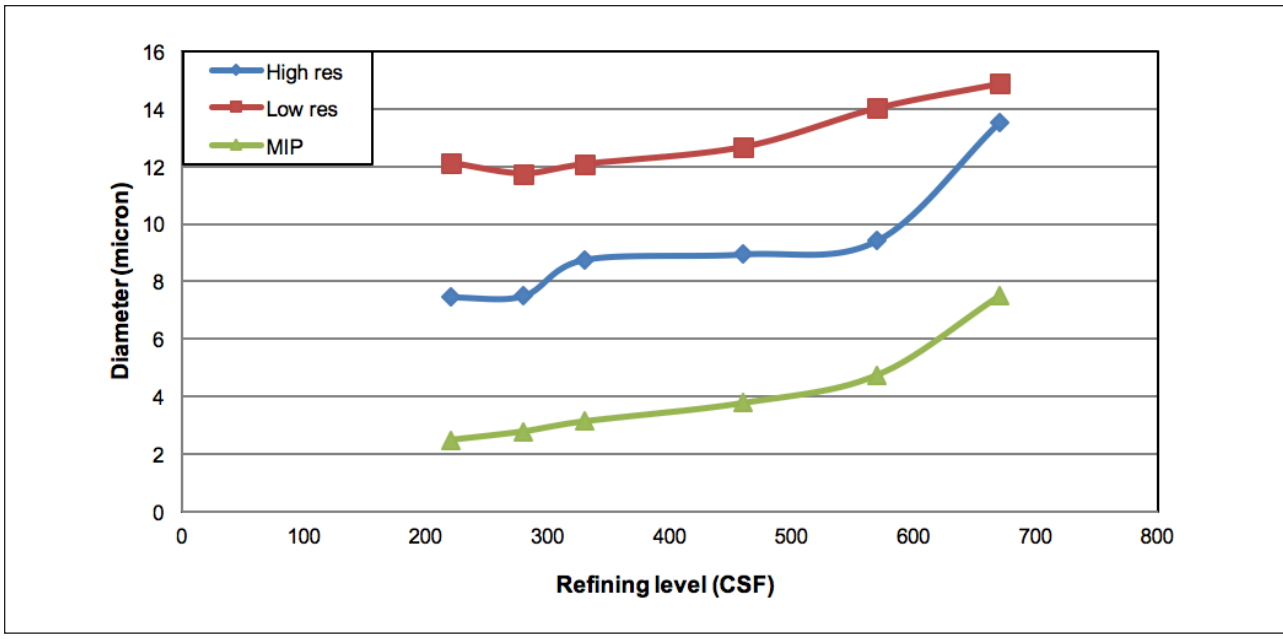

13. Comparison of mean diameters of pores for samples of varying refining levels by different methods.

in porous materials such as paper and board.

Tortuosity

Figure 14 shows the effect of refining on in-plane and transverse geometric tortuosity in paper samples using actual 3D sample volumes. The in-plane tortuosity is lower than the transverse tortuosity in all of the samples because of the layered structure of paper. As the mechanical treatment of fibers is increased, the pores become more tortuous and the geometric tortuosity increases in both the in-plane and transverse directions. The difference in tortuosity between the two orthogonal directions increased with increased refining and sheet consolidation. This could have significant effects on the overall transport and properties of the material and is in agreement with previous work [33].

CONCLUSIONS

X-ray computed tomography is an effective tool to visualize the complex internal 3D microstructure of porous materials. In the current work, paper samples made using different levels of refining or mechanical treatment and from different fiber species are visualized and structural characteristics are determined. The 3D XRCT images at two different resolutions (0.7 μm and 2 μm) were used. To improve the quality of the images and more accurately identify the different material components, a fully automated image processing technique using anisotropic diffusion, minimum error thresholding, isolated voxel removal, and binarization was developed. This technique was applied to paper samples of varying structures and shown to give higher quality images while retaining the essential structural features. Structural characteristics such as porosity, SSA, and 3D pore size distribution were determined using the high resolution XRCT images and compared with experimental methods as well as the low resolution XRCT images reported earlier [30]. Porosity was determined experimentally by sheet caliper and basis area weight measurements. Pore structure characteristics, SSA, and 3D pore size distribution were determined experimentally by MIP. A sphere growing method was developed to compute the 3D pore size distribution using the actual 3D images of sample volumes. This technique is an improvement over the previous 2D pore size distribution technique because it is a combination of the in-plane and transverse pore size distribution and information from neighboring voxels in all three directions is also accounted for.

Porosity results indicate that as the level of refining is increased and the samples are more consolidated, the densities of the paper samples are increased and hence the porosity is decreased. This trend is seen with both experimental data and XRCT image analysis methods. Likewise, the SSA in the dry paper samples containing bonded cellulose fibers is also decreased with an increase in the level of mechanical treatment. Three-dimensional pore size distribution comparisons showed that as the degree of mechanical refining of fibers is increased, the initially larger pores with a wider distribution shift toward smaller pores and narrower distribution. This is expected because of densification and consolidation of the structure and as shown by the porosity data. The MIP technique, which is able to penetrate smaller pore sizes and potential artifacts, showed the smallest pore size distribution followed by 3D high resolution and low resolution XRCT images. In many of the commercial manufacturing and end use applications, structural features from high resolution XRCT images might be adequate in explaining the overall performance. The geometric tortuosity, another important structural characteristic, was also shown to be affected by the

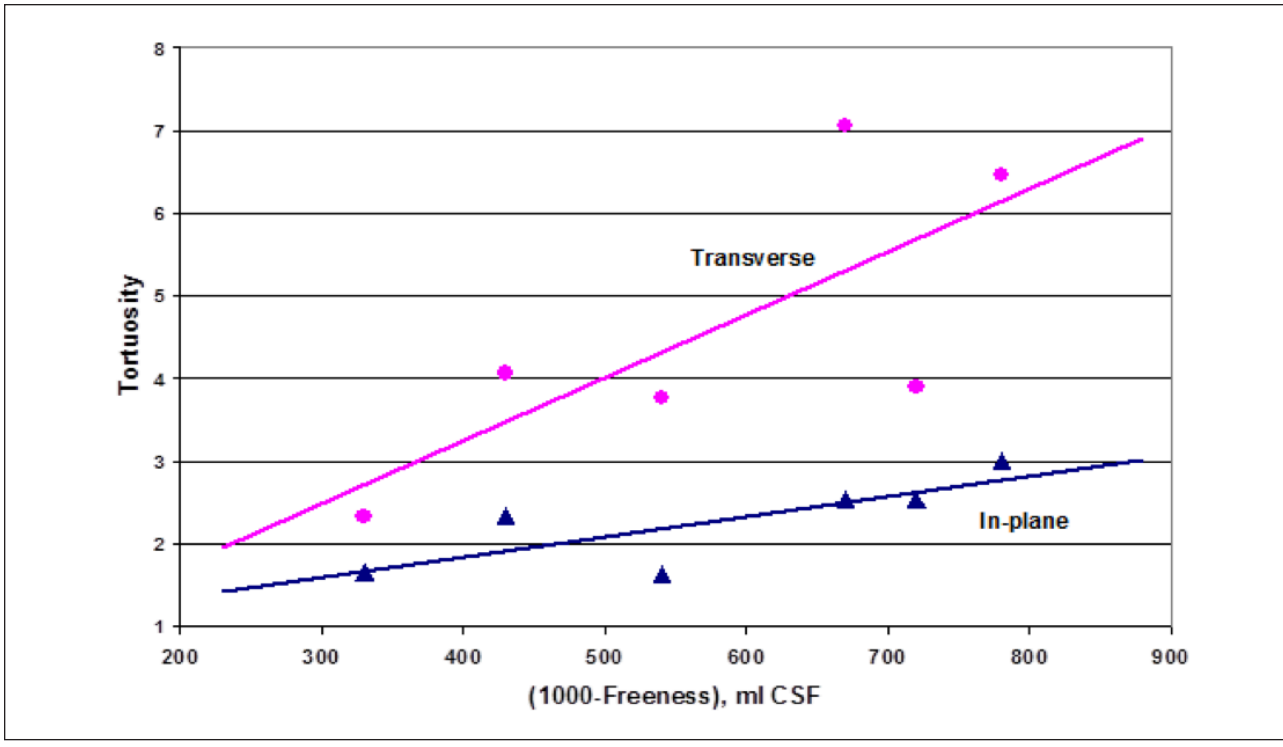

14. Effect of refining on in-plane and transverse geometric tortuosity.

mechanical treatment of fibers. As the mechanical treatment of fibers was increased, with more consolidation and densification of the structure, the pores become more tortuous and the geometric tortuosity increased in both in-plane and transverse directions. The transverse tortuosity was always found to be greater than the in-plane tortuosity, and this could have a significant influence on liquid and vapor transport in the two orthogonal directions.

Given the heterogeneous nature of porous materials such as paper and the relatively small sample volumes used to probe in XRCT technique, it is important to evaluate the material at numerous locations to obtain a more representative characterization. **TJ**

ACKNOWLEDGEMENT

The authors acknowledge the funding support provided by the Minnesota Agriculture Experiment Station and the U.S. Department of Energy.

LITERATURE CITED

1. Modgi, S., Mcquaid, M.E., and Englezos, P., *Nord. Pulp Pap. Res. J.* 21(5): 659(2006).
2. Yang, D., Moran-Mirabal, J.M., Parlange, J.Y., et al., *Biotechnol. Bioeng.* 110(11): 2836(2013).
3. Abrams, L., Favorite, C.W., Capano, P.J., et al., *TAPPI Coat. Conf.*, TAPPI Press, Atlanta, GA, USA, 1996, p. 185.
4. Johnson, R.W., Abrams, L., Maynard, R.B., et al., *TAPPI J.* 82(1): 239(1999).
5. Bloch, J.F., Decain, M., Geindreau, C., et al., *Appita J.* 61(4): 286(2008).
6. Chinga-Carrasco, G., Kauko, H., Myllys, M., et al., *J. Microsc.* 232(2): 212(2008).
7. Van den Bulcke, J., Boone, M., Van Acker, J., et al., *J. Coat. Technol. Res.* 7(2): 271(2010).
8. Mayo, S.C., Chen, F., and Evans, R., *J. Struct. Biol.* 171(2): 182(2010).
9. Du Roscoat, S.R., Bloch, J.F., and Thibault, X., *J. Phys. D: Appl. Phys.* 38(10A): A78(2005).
10. Chinga-Carrasco, G., Axelsson, M., Eriksen, Ø., et al., *J. Pulp Pap. Sci.* 34(1): 13(2008).
11. Samuelsen, E.J., Gregersen, O.W., Houen, P.J., et al., *J. Pulp Pap. Sci.* 27(2): 50(2001).
12. Du Roscoat, S.R., Decain, M., Thibault, X., et al., *Acta Mater.* 55(8): 2841(2007).
13. Van den Bulcke, J., Masschaele, B., Dierick, M., et al., *Int. Biodeterior. Biodegrad.* 61(3): 278(2008).
14. Antoine, C., Nygård, P., Gregersen, Ø.W., et al., *Nucl. Instrum. Methods Phys. Res. Sect. A* 490(1): 392(2002).
15. Saghi, Z. and Midgley, P.A., *Annu. Rev. Mater. Res.* 42: 59(2012).
16. Ramaswamy, S., Huang, S., Goel, A., et al., *12th Fund. Res. Symp.*, The Fundamental Paper Research Society, Bury, U.K., 2001, p. 1281
17. Huang, S., Goel, A., Ramaswamy, S., et al., *Appita J.* 55(3): 230(2002).
18. Goel, A., Tzanakakis, M., Huang, S., et al., *TAPPI J.* 84(5): 72(2001).
19. Defrenne, Y., "Three dimensional structural analysis of porous materials via micro-tomography image processing," Ph.D. dissertation, University of Minnesota, Minneapolis, MN, USA, 2008.

20. Perona, P. and Malik, J., *IEEE Trans. Pattern Anal. Mach. Intell.* 12(7): 629(1990).
21. Kittler, J. and Illingworth, J., *Pattern Recognit.* 19(1): 41(1986).
22. Toriwaki, J. and Yoshida, H., *Fundamentals of Three-dimensional Digital Image Processing*, Springer, New York, 2009, p. 194.
23. Stone, J.E., Scallan, A.M., and Aberson, G.M.A., *Pulp Pap. Mag. Can.* 67(5): T263(1966).
24. Cussler, E.L., *Diffusion: Mass Transfer in Fluid Systems*, Cambridge University Press, New York, 1997, p. 191.
25. Leon, C., *Adv. Colloid Interface Sci.* 76: 341(1998).
26. Romero Morales, E.E., Musso, G., and Jommi, C., in *ALERT Doctoral School 2012: Advanced Experimental Techniques in Geomechanics*, ALERT Geomaterials, Grenoble, 2012, pp. 125-156.
27. Abell, A.B., Willis, K.L., and Lange, D.A., *J. Colloid Interface Sci.* 211(1): 39(1999).
28. Bandyopadhyay, A. and Bose, S., *Characterization of Biomaterials*, Elsevier, Waltham, MA, USA, 2013, p. 41.
29. Washburn, E.W., *Phys. Rev.* 17(3): 273(1921).
30. Goel, A., "Numerical methods and image analysis to predict the transport properties of porous media," Ph.D. thesis, University of Minnesota, St. Paul, MN, USA, 2003.
31. Biermann, C.J., *Handbook of Pulping and Papermaking*, Academic Press, San Diego, CA, USA, 1996, pp. 158-188.
32. Gupta, M.K., "Modeling of simultaneous diffusion in heterogeneous porous media," M.S. thesis, University of Minnesota, St. Paul, 2004.
33. Lindsay, J.D. and Brady, P., "Studies of anisotropic permeability with applications to water removal in fibrous webs," *Nonwovens Conf.*, TAPPI Press, Atlanta, 1992.

ABOUT THE AUTHORS

Three-dimensional (3D) structure of paper and board plays an important role during the manufacturing process and during end-use applications. This study is part of ongoing research on structure-property relationships in porous materials such as paper and board.

In this study, we confirmed that the 3D structure of paper and board is indeed very important and that using the latest scientific developments can help us better understand and "engineer" paper for specific applications. The computational aspects of this work are quite challenging, and we have very good students who helped solve these and other complicated problems.

The most interesting aspect of our study is that it is possible to quantify the 3D internal structure of paper and board and use it for benchmarking products, as well as new process and product development. Mills can use the information here for those purposes, as the technique developed here is already being commercially used.

Our next step is to let mills and technical departments know about the capabilities of this technique and to assist in its widespread use.

Defrenne is process engineer at Appvion Inc., Appleton, WI, USA. Zhdankin is staff engineer at Segate Technology, Shakopee, MN, USA. Ramanna is a doctoral candidate and Ramaswamy is a professor and head of the Department of Bioproducts and Biosystems Engineering, at the University of Minnesota, St. Paul, MN, USA. Ramarao is professor and director, Empire State Paper Research Institute, at the State University of New York College of Environmental Science and Forestry (SUNY-ESF), Syracuse, NY, USA. Email Ramaswamy at shri@umn.edu.

Defrenne

Zhdankin

Ramanna

Ramaswamy

Ramarao